RSC Advances

PAPER

View Article Online
View Journal | View Issue

Cite this: *RSC Adv.*, 2018, **8**, 27587

Adsorption behavior of magnetic bentonite for removing Hg(II) from aqueous solutions†

Chenglong Zou, Jiyan Liang,* Wei Jiang, Yinyan Guan and Yichen Zhang

Bentonite is a porous clay material that shows good performance for adsorbing heavy metals and other pollutants for wastewater remediation. However, it is very difficult to separate the bentonite from water after adsorption as it forms a stable suspension. In this paper, we prepared magnetic bentonite (M-B) by loading Fe_3O_4 particles onto aluminum-pillared bentonite (Al-B) in order to facilitate its removal from water. The functional groups, skeleton structure, surface morphology and electrical changes of the prepared material were investigated by FT-IR, XRD, BET, SEM, VSM and zeta potential measurements. It was used as an adsorbent for Hg(II) removal from aqueous solutions and the influence of various parameters on the adsorption performance was investigated. The adsorption kinetics were best fitted by the pseudo-second-order model, and also followed the intra-particle diffusion model up to 18 min. Moreover, adsorption data were successfully reproduced by the Langmuir isotherm, and the Hg(II) adsorption saturation capacity was determined as 26.18 mg g^{-1}. The average adsorption free energy change calculated by the D-R adsorption isotherm model was 11.89 kJ mol^{-1}, which indicated the occurrence of ionic exchange. The adsorption thermodynamic parameter ΔH was calculated as 42.92 kJ mol^{-1}, which indicated chemical adsorption. Overall, the thermodynamic parameters implied that Hg(II) adsorption was endothermic and spontaneous.

Received 19th June 2018
Accepted 24th July 2018

DOI: 10.1039/c8ra05247f

rsc.li/rsc-advances

1. Introduction

Rapid industrial development has resulted in increased discharge of heavy metal-contaminated wastewater into the environment. This poses a serious safety hazard, owing to the mutagenic, carcinogenic, and teratogenic effects of Hg.[1,2] Hg can enter the human body *via* the inhalation of Hg vapor or the consumption of Hg-contaminated drinking water or fish products.[3,4] The non-biodegradability of Hg results in its accumulation in living organisms, which causes serious health problems such as Minamata disease, kidney failure, and neural disorders.[5,6] Thus, Hg is a primary pollutant that must be closely monitored and controlled in all countries. At present, a number of Hg removal methods have been developed, *e.g.*, chemical precipitation, electrolytic reduction, membrane filtration, reverse osmosis, adsorption, and ion exchange.[6] Among these methods, adsorption shows the most promise because of its high efficiency, convenience, and cost-effectiveness. Bentonite clay is widely used as an adsorbent for wastewater treatment owing to its large surface area, high adsorption capacity, and low cost.[7] However, the separation of bentonite from wastewater is challenging, since this adsorbent swells in water and forms very stable colloidal suspensions.

Magnetic derivatization of adsorbents is a very useful modification of such materials, which has been shown to improve the manipulation.[8,9] By depositing magnetic Fe_3O_4 particles onto the surfaces of adsorbent powder, it can be effectively separated from wastewater using magnetic separation techniques.[10,11] The solvothermal method is effective for preparing high-purity and high-quality magnetic Fe_3O_4 particles with the desired morphology.[12]

In this study, a new low-cost magnetic bentonite (M-B) adsorption material was prepared using the solvothermal method. The functional groups, skeleton structure and surface morphology of the prepared material were analysed by Fourier transform infrared (FT-IR) spectroscopy, X-ray diffraction (XRD), Brunauer–Emmett–Teller (BET) surface area analysis, scanning electron microscopy (SEM), vibrating sample magnetometer (VSM) and zeta potential measurements. And its ability to remove Hg(II) from aqueous solutions was evaluated in detail. In particular, the effects of initial Hg(II) concentration, M-B dosage, pH, and temperature on adsorption performance were studied in detail. Moreover, the adsorption mechanism of interaction between Hg(II) ions and M-B was analysed using a number of kinetic/adsorption isotherm models and thermodynamic analysis. Thus, this study is expected to provide a reference and theoretical basis for the treatment of Hg-containing wastewater with M-B materials.

School of Science, Shenyang University of Technology, Shenyang, 110870, Liaoning, China. E-mail: liangjiy2017@126.com; Tel: +86 24 25497158

† Electronic supplementary information (ESI) available. See DOI: 10.1039/c8ra05247f

2. Experimental

2.1 Materials and reagents

Sodium bentonite (Na-B; Chaoyang City, Liaoning province, China) was crushed and passed through a 200-mesh sieve after purification and air-drying to afford a light yellow powder. Analytical-grade reagents, including $FeCl_3 \cdot 6H_2O$, $AlCl_3 \cdot 6H_2O$, CH_3COONa, $(CH_2OH)_2$, NaOH, HCl, and $HgCl_2$, were purchased from Sinopharm Chemical Reagent Co., Ltd. (China) and used in all experiments. All solutions were prepared using deionized water (18 MΩ cm).

2.2 Preparation of M-B

The Al-B was prepared using a modification of a recently described method at an Al : bentonite ratio of 6 mol kg^{-1}.[13] M-B was prepared by loading magnetic Fe_3O_4 nanoparticles onto Al-pillared bentonite (Al-B) at an Fe : Al-B ratio of 6 mol kg^{-1} using a previously reported solvothermal method.[14]

2.3 Characterization methods

Infrared spectra of the samples were recorded using a Vertex70 FT-IR spectrometer (Thermo Fisher Scientific, USA). The XRD patterns of samples were obtained using a Rigaku D/Max-2550PC diffractometer (Rigaku, Japan), over a diffraction angle (2θ) range of 10–70°, at a scan rate of 4° min^{-1}. SEM images of the nonmagnetic and magnetic samples were taken using an SU8010N and an S-4800 SEM systems (Hitachi, Japan). The N_2 adsorption–desorption isotherms were recorded on a V-Sorb 2800 surface area and porosimetry analyser (Gold APP Instruments Corporation, China). Magnetic characterization was carried out using a magnetic property measurement system (MPMS-7, Quantum Design, USA). zeta potentials of samples in solution were measured by a JS94H zeta potential meter (Powereach, China) at different pH values.

2.4 Batch adsorption experiments

In these experiments, we investigated the effects of parameters such as contact time, pH, temperature, adsorbent dosage, and initial Hg(II) concentrations on adsorption performance. The Hg(II) solution was prepared by dissolving $HgCl_2$ in deionized water in the presence of hydrochloric acid. Batch experiments were carried out in a 500 mL conical flask containing 250 mL of test solution. To adjust pH, 0.1 mol L^{-1} of aqueous HCl or 0.1 mol L^{-1} of aqueous NaOH was added to the test solution, and the flask was then shaken in an electricity-driven thermostatic water bath oscillator at 170 rpm. When the target temperature was reached, the solution was treated with the required amount of M-B. The adsorbent was separated after the desired contact time using an external magnet. All experiments were conducted in triplicate. Hg(II) concentrations were measured by an AAS novAA 400 hydride generation-atomic absorption spectrometer (Analytik Jena AG, Germany).

2.5 Data processing

Hg(II) adsorption efficiencies (r) were calculated using eqn (1):

$$r = \frac{c_0 - c_e}{c_0} \times 100 \quad (1)$$

where c_0 is the initial concentration of Hg(II) (mg L^{-1}), and c_e is the concentration of Hg(II) at adsorption equilibrium (mg L^{-1}).

The Hg(II) adsorption capacity of M-B, which is defined as the amount of Hg(II) adsorbed per gram of M-B (mg g^{-1}), was determined using eqn (2):

$$q_t = \frac{(c_0 - c_t) \times V}{M} \quad (2)$$

where c_t is the concentration of Hg(II) at time t (mg L^{-1}), V is the volume of the solution (L), and M is the dosage of M-B (g). Here, q_t and q_e are the amounts of Hg(II) adsorbed on M-B (mg g^{-1}) at time t and at equilibrium, respectively.

3. Results and discussion

3.1 Characterizations

3.1.1 FT-IR. Changing the structure and surface chemistry of an adsorbent can promote the adsorption processes.[15] The infrared spectra of the samples showed that peak shapes of M-B and Al-B were very similar to those of Na-B (shown in ESI Fig. 1†), indicating that the bentonite structure was not destroyed after modification. The peak at 570 cm^{-1} in the infrared spectrum of M-B was assigned to the characteristic peak of the Fe–O group.[10] The formation of two asymmetric bands between 467 cm^{-1} and 785 cm^{-1} is typical of the spinel structure of Fe_3O_4.[16] These results showed that a covalent bond was formed between the bentonite particles and the Fe_3O_4 particles, indicating that the magnetic Fe_3O_4 particles were successfully loaded onto the Al-B surface to produce M-B.

3.1.2 XRD. The crystal phase of the aluminium oxides and iron oxides between the bentonite layers were analysed using XRD.[12] The results showed that diffraction peaks for bentonite changed only slightly after modification (shown in ESI Fig. 2†), indicating that the crystal shape and structure of the bentonite remained stable. The diffraction peaks at 2θ = 26.65°, 29.5°, 36.54°, and 54.79° were observed for all samples and assigned to silica (SiO_2). The peaks at 19.9°, 35.15°, and 62.24° were assigned to alumina (Al_2O_3), and those peaks of Al-B were enhanced relative to Na-B. The diffraction peaks at 2θ = 30.2°, 35.6°, 43.3°, 53.6°, 57.2°, and 62.90° observed for the M-B sample were assigned to magnetite Fe_3O_4, consistent with the standard peaks for spinel Fe_3O_4 (JCPDS no. 3-863),[16] showing bentonite was successfully loaded with Fe_3O_4. These results were consistent with those of the FT-IR analysis.

3.1.3 Zeta potential. Zeta potential analysis was employed to investigate the electrical changes on the bentonite surface after modification and to provide a reference for further adsorption performance studies. The results are shown in Fig. 1.

As shown in Fig. 1, the point of zero charge (PZC) of Na-B and M-B corresponded to pH 2.4 and pH 3.6, respectively. The electrochemistry on bentonite surface was changed after modification; the zeta potential of M-B became higher than that

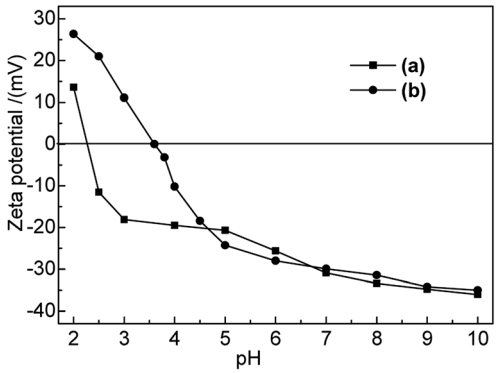

Fig. 1 Zeta potentials of (a) Na-B and (b) M-B in the pH range of 2–10.

of Na-B at pH 2.0–4.7. The zeta potential of M-B was not significantly different with it of Na-B at pH 4.7–10.0.

At pH < pH_{PZC}, M-B exhibited positive zeta potentials, indicating that its surface was positively charged. As pH was increased from 3.6 to 10.0, the functional groups of M-B underwent deprotonation, which decreased its zeta potential from 0 to −35.02 mV and resulted in the build-up of negative surface charge. As a result, the Hg(II) adsorption capacity of M-B increased owing to the electrostatic attraction between Hg(II) ions and the negatively charged M-B surface.

3.1.4 SEM. SEM observations were used to characterize the morphology of the samples (see Fig. 2). The micrographs showed that Na-B consisted of dense particles with closely packed flakes, where the surface had a crumpled microstructure. After modification to produce Al-B, the porosity and roughness of the surface increased, the layers were separated with larger spacing. As shown in the micrographs of Fig. 2(c) and (d), spherical Fe_3O_4 nanoparticles (40–100 nm diameters) were evenly distributed on the bentonite surface. The uniform distribution of Fe_3O_4 nanoparticles with a controlled size was due to vigorous boiling of the solvent during the preparation process.[8] SEM analysis showed the positive effect of modification to produce Al-B and M-B, which is beneficial for their adsorption and separation in wastewater treatment processes.

3.1.5 BET. The adsorption reaction occurs mainly at the surface of solid adsorbents. Hence, the surface structure is a crucial factor determining the adsorption performance. The N_2 adsorption–desorption isotherms and pore size distributions of the adsorbent samples performed are shown in Fig. 3. The specific surface area, mesoporous and microporous pore volumes of the samples are shown in Table 1. As shown in Fig. 3, samples Na-B and Al-B showed type-IV adsorption isotherms with type H_3 hysteresis loops, characteristic of slit-like porous materials. Sample M-B showed typical type-II sorption isotherms, also with type H_3 hysteresis loops, indicating similar pore morphologies to those of the Na-B and Al-B samples. Large hysteresis areas in the N_2 adsorption/desorption isotherms were clearly observed for all samples, suggesting the occurrence of capillary condensation and a wide pore-size distribution.[16] Compared with Na-B, the isotherm of the Al-B sample became steep over the range of P/P_0 of 0.45–0.55, indicating a higher volume of micropores and mesopores.[17] This was consistent

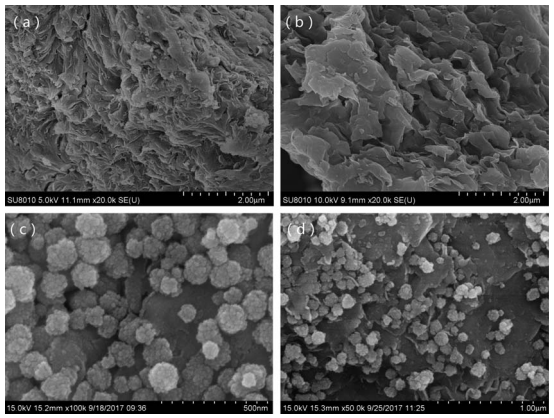

Fig. 2 SEM images of (a) Na-B, (b) Al-B, (c and d) M-B samples.

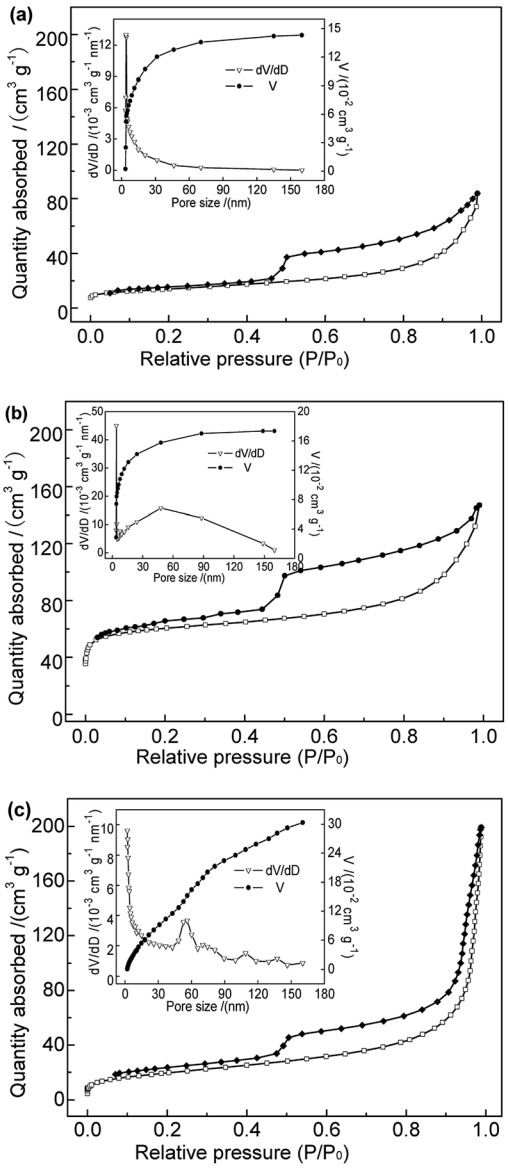

Fig. 3 N_2 adsorption–desorption isotherms and pore size distributions of (a) Na-B, (b) Al-B, and (c) M-B samples.

Table 1 BET parameters of different samples

Samples	Na-B	Al-B	M-B
BET surface area ($m^2\ g^{-1}$)	49.56	206.71	71.35
Microporous surface area ($m^2\ g^{-1}$)	11.35	144.49	3.18
Total pore volume ($cm^3\ g^{-1}$)	0.139	0.174	0.308
Micropore volume ($cm^3\ g^{-1}$)	0.005	0.066	0.001
Average pore size (nm)	10.45	4.40	17.28
Average mesopore size (nm)	6.04	5.47	13.42

with the results shown in Table 1. The BET specific surface area increased from 49.56 $m^2\ g^{-1}$ to 206.71 $m^2\ g^{-1}$; this was related to the expansion of the bentonite layer spacing and the mesoporosity introduced during the synthesis of Al-B. The total average pore size and average mesopore of Al-B were both smaller than those of Na-B. Considering the P/P_0 range of 0.45–0.55 the isotherm of M-B was lightly smoother than those of Na-B and Al-B, consistent with the lower microporosity. Table 1 shows the significant decrease in specific surface area and pore area of M-B compared to Al-B, especially the micropore area and volume (which reduced to nearly zero). The total average pore size and average mesopore size of M-B both increased compared to Al-B. This is probably due to Fe_3O_4 particles penetrating the bentonite layers and pore channels, covering the surface. This provides more evidence that the Fe_3O_4 particles were successfully grafted onto the bentonite surface. Further systematic studies are required to determine the effect of the pore volume on the adsorption behavior.

3.1.6 Magnetic properties. The magnetic characterization results showed magnetization saturation value for M-B of 22.08 emu g^{-1} (shown in ESI Fig. 3†). Such a high magnetization was related to the morphology of the Fe_3O_4 nanoparticles on the bentonite surface developed during the preparation process. In addition, the magnetic remanence and hysteresis were nearly zero, consistent with a soft magnetic material and indicating superparamagnetic behavior. The high saturation magnetization and superparamagnetic behavior allowed the M-B suspended in water to be quickly separated from the dispersion with a magnet. After the magnetic field was removed, the M-B quickly dispersed in the solution again. Aggregation between the particles did not occur with the applied magnetic field.

3.2 Adsorption properties

3.2.1 Effect of contact time and adsorption kinetics. Contact time, an important factor that determines the equilibration rate,[18] was investigated in the range of 0–18 min at 35 °C, pH 7, initial Hg(II) concentration of 50 mg L^{-1}, and an M-B dosage of 4.0 g L^{-1}. The results (Fig. 4(a)) indicated that Hg(II) binding was rapid, *i.e.*, an adsorption efficiency of 71.96% was reached within the first 3 min of contact. Furthermore, the maximum adsorption capacity was reached after 18 min, corresponding to an adsorption efficiency of 98.78%. Notably, adsorption did not increase with further increase in contact time. However, it was found that it took nearly 30 min to reach absorption equilibrium at low temperatures. Therefore, 30 min was selected as the optimum contact time for subsequent experiments.

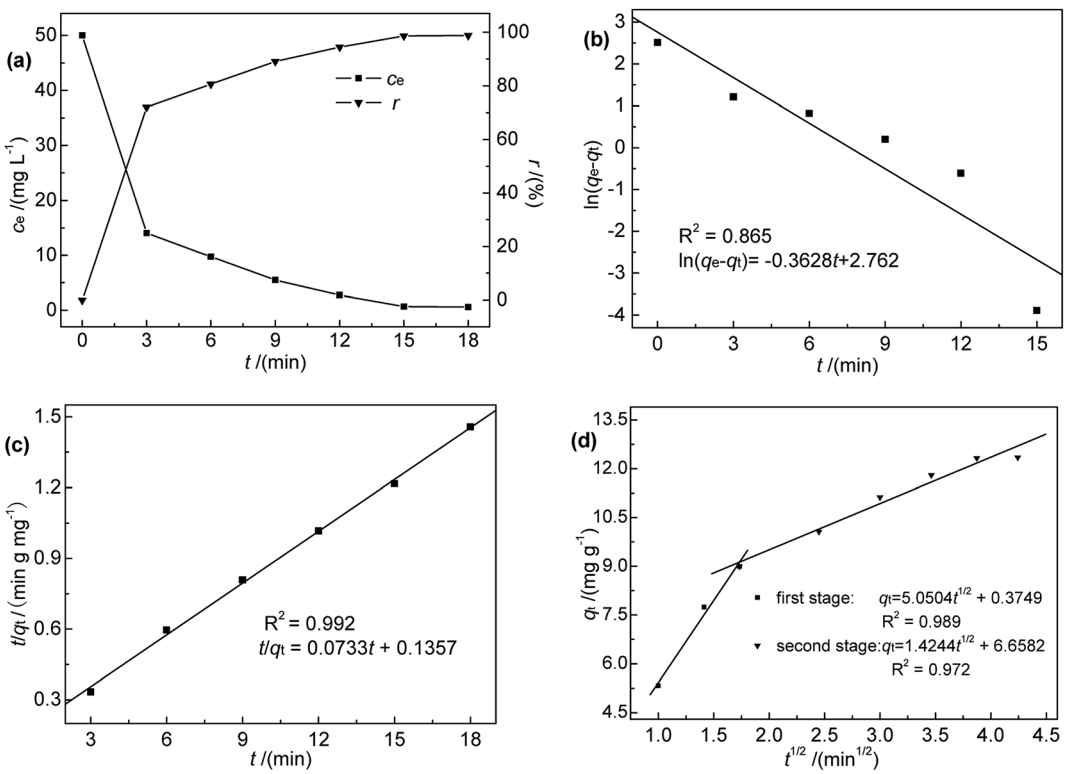

Fig. 4 (a) Effect of contact time on c_e and r; (b) pseudo-first-order, (c) pseudo-second-order, and (d) intra-particle diffusion kinetic model fits for Hg(II) adsorption onto M-B (c_0 = 50 mg L^{-1}, pH 7.0, M-B dosage = 4 g L^{-1}, temperature = 35 °C).

To further explore the rate-controlling steps of adsorption and its dynamic characteristics, experimental data were fitted by Lagergren pseudo-first-order and pseudo-second-order kinetic models using the linear equations provided below (eqn (3) and (4)).[19] The intra-particle diffusion model proposed by Weber and Morris was applied to analyse the rate-controlling step of adsorption and describe localized adsorption for specific interactions (eqn (5)).[20]

$$\ln(q_e - q_t) = \ln q_e - k_1 t \quad (3)$$

$$\frac{t}{q_t} = \frac{1}{k_2 q_e^2} + \frac{1}{q_e} t \quad (4)$$

$$q_t = k_3 t^{1/2} + C \quad (5)$$

where k_1, k_2 and k_3 are the pseudo-first-order rate constant (min^{-1}), pseudo-second order (g mg^{-1} min^{-1}) rate constant and intra-particle diffusion rate constant (mg g^{-1} $min^{-1/2}$), respectively. C is the intercept constant (mg g^{-1}).

The fits obtained using eqn (3)–(5) are shown in Fig. 4(b)–(d), and the adsorption capacities and rate constants calculated from these plots are listed in Table 2. The results showed that experimental kinetic data were best fitted by the pseudo-second-order model, which also provided a better prediction of the equilibrium adsorption capacity. As the main adsorption-affecting factor of the pseudo-second-order model is the interaction of M-B functional groups with Hg(II), the above findings suggested the occurrence of chemical adsorption.

The fitting adsorption curve of intra-particle diffusion model (Fig. 4(d)) showed two distinct adsorption processes. The first step was related to Hg(II) adsorption on active sites on the surface of M-B (surface adsorption process), while the second step was related to Hg(II) diffusion absorption in the pores of M-B (particle diffusion process). The intercept C of the particle diffusion process was not equal to zero. Hence, the adsorption process was not only controlled by particle diffusion, which is consistent with the analysis of pseudo-second order kinetic.[20]

3.2.2 Effect of pH. pH is known to be the most important variable governing the adsorption of heavy metals onto various materials.[21,22] It greatly affects the adsorbent surface charge and the metal speciation in solution, while solvated protons themselves can strongly compete with metal ions for adsorption sites.[23,24] Generally, acidic conditions are believed to be unfavourable for the adsorption of heavy metal ions on bentonite, in contrast to neutral and alkaline ones.[25] In this research, the effects of pH on the adsorption of Hg(II) were investigated in the range of 2–9 at 35 °C. The initial Hg(II) concentration, M-B dosage, and contact time were kept constant at 50 mg L^{-1}, 4.0 g L^{-1}, and 30 min, respectively.

As shown in Fig. 5, the removal efficiency of Hg(II) was significantly affected by pH. A rapid and continuous decrease in c_e was observed with increasing pH, whereas r steadily increased, reaching a maximum (99.52%) at pH 8 and decreasing slightly thereafter. The above finding was explained as follows. At low pH, Hg^{2+} ions were the dominant species in the solution and were repelled by the positively charged M-B surface. Additionally, the H_3O^+ ions abundantly present in solution at low pH strongly competed with Hg(II) ions for adsorption sites on the M-B surface,[26] effectively decreasing the amount of adsorbed Hg^{2+} ions.

At pH 3.6–7.0, the solution mainly contained $Hg(OH)^+$ and $Hg(OH)_2$ (with hydrated sizes exceeding that of Hg^{2+}) that were strongly bound by the adsorption sites of the sorbent surface, which resulted in enhanced Hg(II) removal efficiency.[27,28] At pH > pH_{PZC}, more metal-binding sites on the negatively charged M-B surface were exposed, whereas a certain fraction of Hg(II) in solution was still present as positively charged ions. These conditions favoured the interaction between Hg(II) and the active groups on the M-B surface. With increasing pH, the above interaction was strengthened owing to the concomitantly increasing electronegativity of M-B, which increased its Hg(II) adsorption capacity. However, a further increase in pH to 9 decreased the amount of adsorbed Hg(II) species, which was attributed to the deposition of Hg(II) as $Hg(OH)_2$ (K_{sp} $Hg(OH)_2$ = 3.13×10^{-26}). Finally, excessively high pH values promoted the formation of negatively charged Hg(II)–OH complexes that were electrostatically repelled by the strongly negatively charged M-B surface.[29] Therefore, pH 7.0 was selected as the optimal condition.

3.2.3 Effect of adsorbent dosage. The effects of Na-B and M-B dosage on the efficiency of Hg(II) removal were explored for

Table 2 Kinetic parameters obtained for Hg(II) adsorption onto M-B

Pseudo-first order		Pseudo-second order	
$q_{e,exp}$ (mg g^{-1})	12.35	$q_{e,exp}$ (mg g^{-1})	12.35
$q_{e,cal}$ (mg g^{-1})	15.831	$q_{e,cal}$ (mg g^{-1})	13.643
k_1 (min^{-1})	0.3628	k_2 (g mg^{-1} min^{-1})	0.0396
R^2	0.865	R^2	0.992
Intra-particle diffusion			
		First step	Second step
C (mg g^{-1})		0.375	6.658
k_3 (mg g^{-1} $min^{-1/2}$)		5.050	1.424
R^2		0.989	0.972

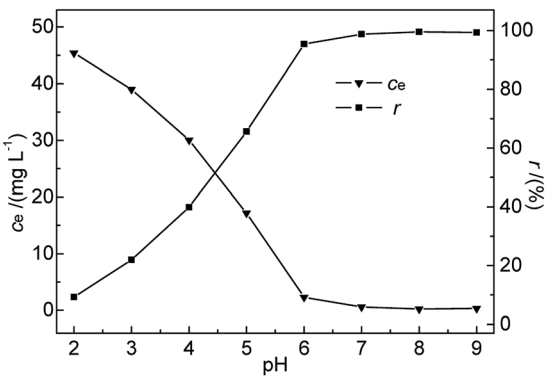

Fig. 5 Effect of pH on c_e and r (c_0 = 50 mg L^{-1}, M-B dosage = 4 g L^{-1}, temperature = 35 °C, contact time = 30 min).

adsorbent dosages of 1.0–6.0 g L^{-1} at 35 °C, pH 7, initial Hg(II) concentration of 50 mg L^{-1}, and a contact time of 30 min. The results are shown in Fig. 6.

Fig. 6 shows that the adsorption efficiency and adsorption capacity of M-B were significantly higher than that of Na-B with the dosages range 1.0 to 3.0 g L^{-1}. The results indicated that the adsorption performance was improved after modification, which might be due to the several following reasons. After modification, the specific surface area and the total pore volume of bentonite increased, contributing to the active points on the surface increased. Compared with Na-B, the pore size of M-B increased, which was beneficial for the diffusion of particles.

The efficiency of Hg(II) removal sharply increased as the M-B dosage was increased from 1.0 to 4.0 g L^{-1}, which was ascribed to the increasing number of binding sites. Further increases in M-B dosage did not have a significant effect, which was attributed to the insufficient residual metal concentration in solution.[30] In addition, the adsorption process followed isothermal adsorption equilibrium theory.

3.2.4 Effect of initial Hg(II) concentration and adsorption isotherms. As we know, bentonite materials are always used for adsorption treatment of pollutants in industrial wastewater.[7] In order to be effective, the adsorption-based removal of contaminants must be carried out within a suitable contaminant concentration range. Since the initial concentration of metal ions in solution determines the magnitude of the driving force required to overcome the mass transfer resistance between aqueous and solid phases in batch experiments.[31] Based on the references to a number of related literatures[7,12,28] and our preliminary experiments, the effect of initial concentration was studied at 35 °C and pH 7 for initial Hg(II) concentrations of 10.0–60.0 mg L^{-1}. The M-B dosage and contact time were fixed at 4.0 g L^{-1} and 30 min, respectively. The results are shown in Fig. 7.

As shown in Fig. 7, the amount of adsorbed Hg(II) increased from 2.48 to 14.79 mg g^{-1} when the initial Hg(II) concentration was increased from 10.0 to 60.0 mg L^{-1}. This increase was almost linear, which was ascribed to the fact that the equilibrium adsorption capacity was lower than the saturated adsorption capacity. However, r slightly decreased with increasing initial Hg(II) concentration. The prepared M-B exhibited a high Hg(II) adsorption ability, although it was difficult to achieve the Hg(II) concentration limit (GB 8978-1996) for high-concentration wastewater with batch-type adsorption. Thus, M-B was concluded to be well suited for the pre-treatment of wastewater contaminated with high concentrations of Hg(II).

To shed further light on the distribution of Hg(II) between the liquid and solid phases at equilibrium, the equilibrium data (amounts of Hg(II) adsorbed per gram of M-B and the equilibrium concentrations of Hg(II); shown in Fig. 8(a)) were fitted using Langmuir and Freundlich isotherms (eqn (6) and (7), respectively).[32,33]

$$\frac{q_e}{c_e} = \frac{1}{K_L Q} + \frac{C_e}{Q} \quad (6)$$

$$\ln q_e = \ln K_F + \frac{1}{n} \ln c_e \quad (7)$$

where Q is the Langmuir monolayer adsorption capacity (mg g^{-1}), K_L is the Langmuir constant (L g^{-1}), and K_F and n are the Freundlich constants referring to the adsorption capacity and adsorption intensity, respectively.

Fig. 8(b) and (c) show the fits obtained for the above models, indicating that the adsorption of Hg(II) on M-B was best modelled by the Langmuir isotherm. It suggested that this adsorption corresponded to monolayer coverage of Hg(II) on the surface of M-B.[34] In addition, the adsorption saturation capacity was determined as 26.18 mg g^{-1}. The value of $1/n = 0.707$ ($0 < 1/n < 1$) was indicative of a material with a heterogeneous surface

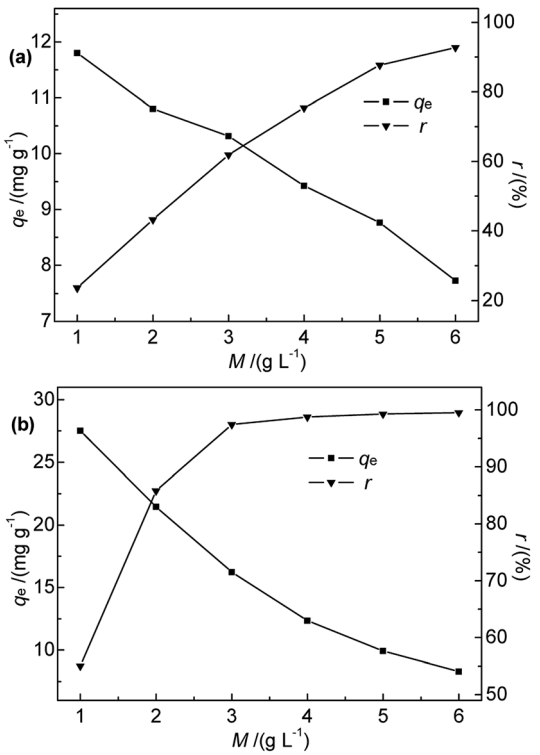

Fig. 6 Effect of (a) Na-B and (b) M-B dosage on q_e and r (c_0 = 50 mg L^{-1}, pH = 7, temperature = 35 °C, contact time = 30 min).

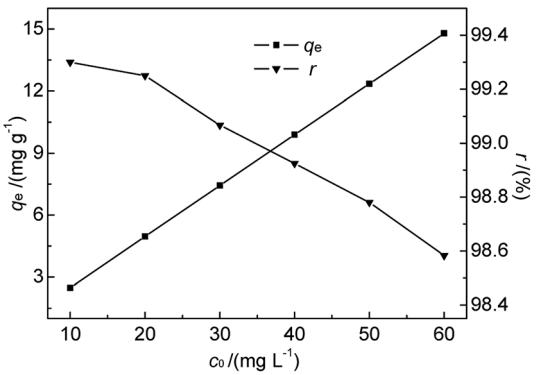

Fig. 7 Effect of initial Hg(II) concentration on q_e and r (M-B dosage = 4 g L^{-1}, pH = 7, temperature = 35 °C, contact time = 30 min).

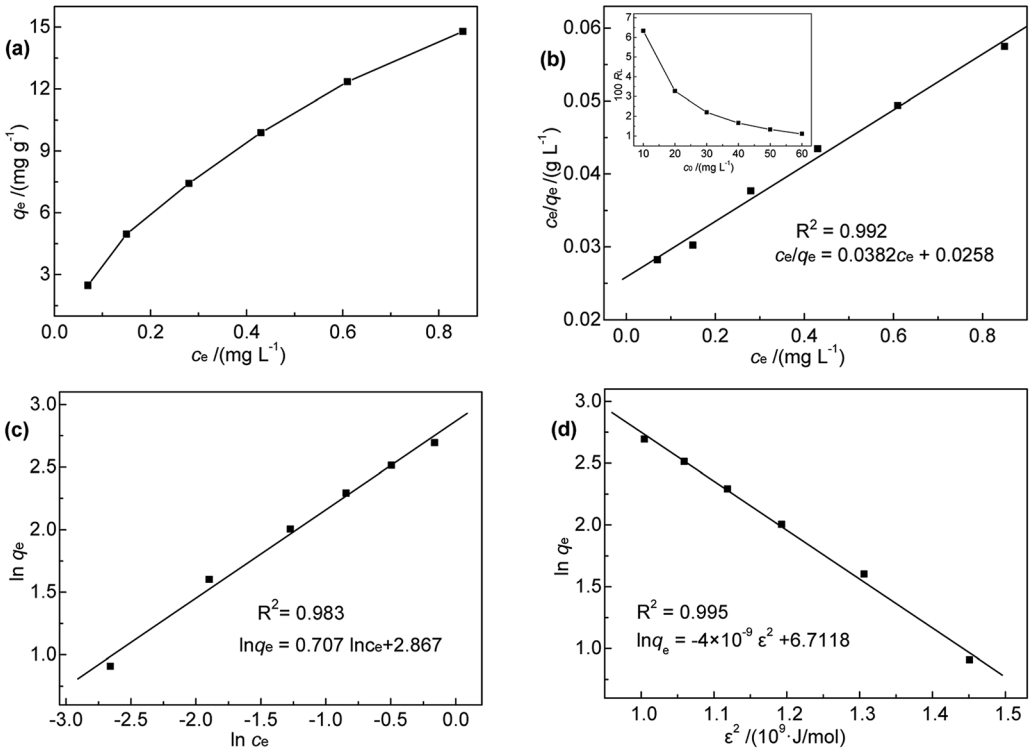

Fig. 8 (a) Relationship between q_e and c_e; (b) Langmuir, (c) Freundlich, and (d) D-R isotherms for Hg(II) adsorption onto M-B.

structure featuring an exponential distribution of active sites. In addition, the high value of Freundlich adsorption constant demonstrated the strong affinity of M-B toward Hg(II).[35]

The essential characteristics of the Langmuir isotherm can be expressed by a dimensionless constant known as the equilibrium parameter (R_L) (eqn (8)).[36]

$$R_L = \frac{1}{1 + k_L C_0} \quad (8)$$

Based on the magnitude of R_L, isotherms can be classified as those representing irreversible ($R_L = 0$), favourable ($0 < R_L < 1$), linear ($R_L = 1$), or unfavourable ($R_L > 1$) adsorption.[37] In this work, K_L was calculated as 0.131 L mg^{-1} (shown in Table 3). When the initial Hg(II) concentration was increased from 10.0 to 60.0 mg L^{-1}, the R_L values (shown in Fig. 8(b)) indicated that Hg(II) ions were favourably adsorbed by M-B.

Additionally, the adsorption mechanism can be deduced from the average adsorption free energy (E_s). The magnitude of E_s indicates physical adsorption (when the value of E_s is lower than 8 kJ mol^{-1}), chemical adsorption (when the value of E_s is higher than 16 kJ mol^{-1}) and the presence of ionic exchange (for range between 8 and 16 kJ mol^{-1}).[38] The E_s is calculated using the Dubinin-Radushkevich (D-R) adsorption isotherm model (eqn (9)–(11)):[39]

$$\ln q_e = \ln q_m - k_d \varepsilon^2 \quad (9)$$

$$\varepsilon = RT \ln\left(1 + \frac{1}{c_{e2}}\right) \quad (10)$$

$$E_s = \frac{1}{\sqrt{2k_d}} \quad (11)$$

where q_m is the maximal adsorption capacity (mg g^{-1}), c_{e2} is the Hg(II) concentration at equilibrium (mol L^{-1}), k_d is a constant (mol^2 J^{-2}), T is the temperature (K), R is the universal gas constant (8.3145 J mol^{-1} K^{-1}), and ε is the Polanyi potential (J mol^{-1}).

The fits obtained using the linear equation of the D-R model is shown in Fig. 8(d). Based on the obtained k_d value, E_s was calculated as 11.89 kJ mol^{-1} using eqn (11). The fact that this value was in the range of 8–16 kJ mol^{-1} indicated the occurrence of ionic exchange during adsorption process.[38,40]

3.2.5 Effect of temperature and adsorption thermodynamics. Reaction temperature is known to affect adsorption efficiency.[41] In this research, adsorption experiments were performed at temperatures of 10–50 °C, and the initial concentration of Hg(II), M-B dosage, pH, and contact time were fixed at 50 mg L^{-1}, 4 g L^{-1}, 7, and 30 min, respectively. The temperature dependences of c_e and r are shown in Fig. 9(a).

Table 3 Langmuir, Freundlich, and D-R isotherm model parameters of Hg(II) adsorption onto M-B

Langmuir		Freundlich		D-R	
K_L (L mg^{-1})	1.481	K_F	17.584	q_m (mg g^{-1})	822.05
Q (mg g^{-1})	26.18	n	1.414	E_s (kJ mol^{-1})	11.89
R^2	0.992	R^2	0.983	R^2	0.995

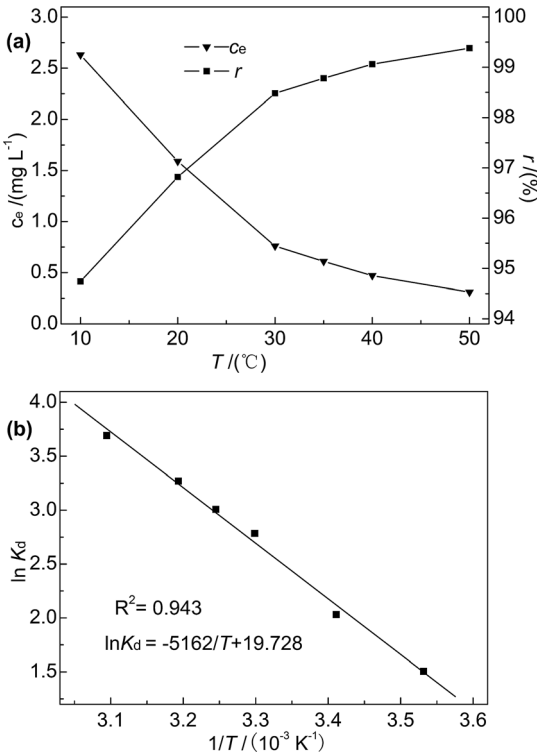

Fig. 9 (a) Effect of temperature on r and c_e; (b) plot of ln K_d *versus* 1/T.

As the temperature increased from 10 to 50 °C, the Hg(II) removal rate slightly increased (from 94.74% to 99.38%), and the Hg(II) equilibrium adsorption capacity and residual concentration at 50 °C were determined as 12.42 mg g^{-1} and 0.31 mg L^{-1}, respectively. This finding indicated that the adsorption of Hg(II) onto M-B was favoured at high temperature, which suggested that the adsorption process was endothermic. Moreover, thermodynamic analysis revealed the occurrence of chemisorption, the extent of which is known to increase with increasing temperature because of the concomitant facilitation of diffusion.[42] In contrast, the reaction temperature had little influence on the adsorption efficiency, which was in agreement with previously obtained results.[36]

The effect of temperature on Hg(II) adsorption was further studied by thermodynamic analysis using eqn (12)–(15) to determine changes in the Gibbs free energy (ΔG), enthalpy (ΔH), and entropy (ΔS):[43,44]

$$K_d = \frac{q_e}{c_e} \quad (12)$$

$$\ln K_d = \frac{\Delta S}{R} - \frac{\Delta H}{RT} \quad (13)$$

$$\Delta G = \Delta H - T\Delta S \quad (14)$$

$$\Delta G = -RT \ln K_d \quad (15)$$

where K_d is the adsorption distribution constant (L g^{-1}).

ΔH and ΔS were obtained from the plot of ln K_d *vs.* 1/T (Fig. 9(b)), which allows for the determination of ΔG. Table 4 lists the obtained thermodynamic parameters and the calculated correlation coefficients, and shows that the adsorption ΔH was positive and exceeded 40 kJ mol^{-1}. This indicated that the adsorption of Hg(II) onto M-B was endothermic and chemical in nature. The positive value of ΔS suggested that adsorption increased randomness at the solid–liquid interface and reflected the affinity of M-B for Hg(II).[37] The ΔG values were negative and decreased with increasing temperature, which indicated that adsorption was spontaneous in nature. Furthermore, the increase in $|\Delta G|$ with increasing temperature suggested that the adsorption of Hg(II) onto M-B was more favourable at higher temperatures.[45]

Table 4 Thermodynamic parameters of Hg(II) adsorption onto M-B

T (K)	ΔG (kJ mol^{-1})	ΔH (kJ mol^{-1})	ΔS (J mol^{-1} K^{-1})
283	−3.54	42.92	164.03
293	−4.94		
303	−7.02		
308	−7.70		
313	−8.51		
323	−9.91		

4. Conclusions

Magnetic bentonite was prepared in this study and characterized. The results showed that the bentonite structure was not destroyed during the process of modification. The porosity and roughness of the surface increased, and the layers are separated with larger spacing after modification. Fe_3O_4 spherical nanoparticles were evenly distributed on the surface of Al-B with sizes of ~40–100 nm. M-B was superparamagnetic with a magnetization saturation value of 22.08 emu g^{-1}.

It was successfully used as an adsorbent to remove Hg(II) from aqueous solutions. The effects of several parameters on adsorption capacity and efficiency were studied. Notably, M-B was shown to be an effective Hg(II) adsorbent. Under the optimized conditions (pH 8, contact time = 30 min, temperature = 35 °C, initial Hg(II) concentration = 50 mg L^{-1}, M-B dosage = 4.0 g L^{-1}), the residual concentration and removal efficiency of Hg(II) were determined as 0.24 mg L^{-1} and 99.52%, respectively.

The adsorption process was best fitted by a pseudo-second-order kinetic model; it followed the intra-particle diffusion model up to 18 min. The Langmuir model was successfully applied to fit the adsorption data, allowing the saturation Hg(II) adsorption capacity of M-B to be calculated as 26.18 mg g^{-1}. Moreover, the adsorption process mainly corresponded to chemical adsorption and ionic exchange. Thermodynamic analysis demonstrated that the adsorption process was endothermic and spontaneous, and was therefore favoured by high temperatures. Thus, M-B was concluded to be a promising low-cost adsorbent for the efficient removal of Hg(II) from liquid waste.

Conflicts of interest

There are no conflicts to declare.

Acknowledgements

This work was financially supported by the China Environmental Protection Foundation, Geping Green Action, Liaoning Environmental Research and Education Fund "123 Project" (Grant No. CEPF2014-123-1-6). And, this work was sponsored by "Liaoning BaiQianWan Talents Program".

References

1 J. O. Nriagu and J. M. Pacyna, *Nature*, 1988, **333**, 134–139.
2 R. J. Lu, J. A. Hou, J. Xu, T. M. Tang and X. H. Xu, *J. Hazard. Mater.*, 2011, **196**(1), 160–165.
3 S. C. Foo and T. C. Tan, *Sci. Total Environ.*, 1998, **209**, 185–192.
4 T. M. Tang, J. Xu, R. J. Lu, J. J. Wo and X. H. Xu, *Fuel*, 2010, **89**(12), 3613–3617.
5 M. F. Wolfe, S. Schwarzbach and R. A. Sulaiman, *Environ. Toxicol. Chem.*, 2010, **17**, 146–160.
6 T. W. Clarkson and L. Magos, *Crit. Rev. Toxicol.*, 2006, **36**, 609–662.
7 J. Shu, Y. Peng, C. D. Pan, X. Z. Cheng and L. Deng, *Adv. Mater. Res.*, 2013, **781–784**, 1977–1980.
8 F. L. Fu and Q. Wang, *J. Environ. Manage.*, 2011, **92**, 407–418.
9 J. Xu, X. Liu, G. V. Lowry, Z. Cao, H. Zhao, J. L. Zhou and X. H. Xu, *ACS Appl. Mater. Interfaces*, 2016, **8**, 7333–7342.
10 A. Mockovciaková, Z. Orolínová and J. Skvarla, *J. Hazard. Mater.*, 2010, **180**, 274–281.
11 K. Chen, G. Wang, W. B. Li, D. Wan, Q. Hu, L. L. Lu, X. B. Wei and Z. Z. Chen, *J. Wuhan Univ. Technol., Mater. Sci. Ed.*, 2015, **30**, 302–306.
12 L. S. Tan, J. Xu, X. Q. Xue, Z. M. Lou, J. Zhu, S. A. Baig and X. H. Xu, *RSC Adv.*, 2014, **86**, 45920–45929.
13 V. Cabuil, V. Dupuis, D. Talbot and S. Neveu, *J. Magn. Magn. Mater.*, 2011, **323**, 1238–1241.
14 L. Lian, X. Cao, Y. Q. Wu, D. Z. Sun and D. W. Lou, *Appl. Surf. Sci.*, 2014, **289**, 245–251.
15 T. K. Sen and D. Gomez, *Desalination*, 2011, **267**, 286–294.
16 J. H. Meng, G. Q. Yang, L. M. Yan and X. Y. Wang, *Dyes Pigm.*, 2005, **66**, 109–113.
17 W. B. Guan, B. X. Zhao, S. Qiu, N. Liu, L. Niu, R. Cheng and Y. Sun, *J. Northwest Univ.*, 2016, **46**, 375–380.
18 Q. H. Wang, X. J. Chang, D. D. Li, Z. H. Hu, R. J. Li and Q. He, *J. Hazard. Mater.*, 2011, **186**, 1076–1081.
19 A. D. Monfared, M. H. Ghazanfari, M. Jamialahmadi and A. Helalizadeh, *Chem. Eng. J.*, 2015, **281**, 334–344.
20 N. Sun, W. Shi, L. Ma and S. Yu, *RSC Adv.*, 2017, **7**(28), 17095–17106.
21 A. S. Özcan, Ö. Gök and A. Özcan, *J. Hazard. Mater.*, 2009, **161**, 499–509.
22 S. Vilvanathan and S. Shanthakumar, *Environ. Technol.*, 2017, **39**(4), 1–42.
23 M. M. Liu, L. A. Hou, B. D. Xi, Y. Zhao and X. F. Xia, *Appl. Surf. Sci.*, 2013, **273**, 706–716.
24 A. Sari, M. Tuzen, D. Citak and M. Soylak, *J. Hazard. Mater.*, 2007, **148**, 387–394.
25 J. Shi, Z. B. Zhao, Z. J. Liang and T. Y. Sun, *Water Sci. Technol.*, 2016, **73**, 2422–2429.
26 G. Blázquez, M. A. Martín-Lara, E. Dionisio-Ruiz, G. Tenorio and M. Calero, *J. Ind. Eng. Chem.*, 2012, **18**, 1741–1750.
27 P. Hadi, M. H. To, C. Hui, C. S. K. Lin and G. Mckay, *Water Res.*, 2015, **73**, 37–55.
28 N. Sun, X. Wen and C. J. Yan, *Int. J. Biol. Macromol.*, 2017, **108**, 1199–1206.
29 M. Mudasir, K. Karelius, N. H. Aprilita and E. T. Wahyuni, *J. Environ. Chem. Eng.*, 2016, **4**, 1839–1849.
30 D. Hamane, O. Arous, F. Kaouah, M. Trari, H. Kerdjoudj and Z. Bendjama, *J. Environ. Chem. Eng.*, 2015, **3**, 60–69.
31 R. R. Pawar, B. H. C. Lalhmunsiama and S. M. Lee, *J. Ind. Eng. Chem.*, 2016, **34**, 213–223.
32 Y. He, Y. G. Chen and W. M. Ye, *Environ. Earth Sci.*, 2016, **75**, 807.
33 N. Xue, L. Wang, M. Pei, Y. He, Y. Du and W. Guo, *RSC Adv.*, 2016, **6**(101), 98945–98951.
34 Y. H. Song, M. C. Lu, B. Huang, D. L. Wang, G. Wang and L. Zhou, *J. Alloys Compd.*, 2018, **737**, 113–121.
35 Q. X. Yao, J. J. Xie, J. X. Liu, H. M. Kang and Y. Liu, *J. Polym. Res.*, 2014, **21**, 465.
36 M. Hamidpour, M. Kalbasi, M. Afyuni, H. Shariatmadari and G. Furrer, *Environ. Earth Sci.*, 2011, **62**, 559–568.
37 Q. Kang, W. Z. Zhou, Q. Li, B. Y. Gao, J. X. Fan and D. Z. Shen, *Appl. Clay Sci.*, 2009, **45**, 280–287.
38 M. L. Cantuaria, A. F. D. A. Neto, E. S. Nascimento and M. G. A. Vieira, *J. Cleaner Prod.*, 2015, **112**, 1112–1121.
39 Y. G. Chen, Z. Sun, W. M. Ye and Y. J. Cui, *J. Radioanal. Nucl. Chem.*, 2017, **311**, 1839–1847.
40 M. D'Arcy, D. Weiss, M. Bluck and R. Vilar, *J. Colloid Interface Sci.*, 2011, **364**, 205–212.
41 I. Daou, O. Zegaoui and A. Amachrouq, *Water Sci. Technol.*, 2017, **75**, 1098–1117.
42 K. K. Anoop and T. S. Anirudhan, *J. Hazard. Mater.*, 2002, **92**, 161–183.
43 S. M. Awadh and F. H. Abdulla, *Environ. Earth Sci.*, 2017, **76**, 386.
44 H. Chen, Q. S. Chen, B. Huang, S. W. Wang and L. Y. Wang, *J. Radioanal. Nucl. Chem.*, 2018, **316**, 71–80.
45 H. Moussout, H. Ahlafi, M. Aazza, O. Zegaoui and A. C. El, *Water Sci. Technol.*, 2016, **73**, 2199–2210.